High-Permittivity Pad Design for Dielectric Shimming in Magnetic Resonance Imaging Using Projection-Based Model Reduction and a Nonlinear Optimization Scheme

van Gemert, J.H.F.; Brink, W.M.; Webb, A.G.; Remis, R.F.

DOI
10.1109/TMI.2018.2791179

Publication date
2018

Document Version
Accepted author manuscript

Published in
IEEE Transactions on Medical Imaging

High-Permittivity Pad Design for Dielectric Shimming in Magnetic Resonance Imaging using Projection Based Model Reduction and a Nonlinear Optimization Scheme

J.H.F. van Gemert, W.M. Brink, A.G. Webb, and R.F. Remis

***Abstract*—Inhomogeneities in the transmit RF magnetic field (B_1^+) reduce the quality of MR images. This quality can be improved by using high-permittivity pads that tailor the B_1^+ fields. The design of an optimal pad is application-specific and not straightforward, and would therefore benefit from a systematic optimization approach. In this paper, we propose such a method to efficiently design dielectric pads. To this end, a projection based model order reduction technique is used that significantly decreases the dimension of the design problem. Subsequently, the resulting reduced order model is incorporated in an optimization method in which a desired field in a region of interest can be set. The method is validated by designing a pad for imaging the cerebellum at 7T. The optimal pad that is found is used in an MR measurement to demonstrate its effectiveness in improving the image quality.**

***Index Terms*—Magnetic resonance imaging, dielectric shimming, high-permittivity pads, B_1^+ fields, reduced order modeling, optimization**

I. Introduction

MAgnetic Resonance Imaging (MRI) is a non-invasive technique that can be used to create detailed images of the anatomy of the human body. The signal-to-noise ratio (SNR) of these images can be significantly improved by using higher static magnetic fields, which in turn enables reduced scan times and MR images with a higher spatial resolution [1]. The frequency of the radiofrequency (RF) excitation field that is used for MR imaging is linearly related to the magnitude of the static magnetic field, explicitly

$$f = \gamma B_0, \tag{1}$$

where γ [Hz/T] is the gyromagnetic ratio and B_0 the magnitude of the static field. For ^{1}H the gyromagnetic ratio is $\gamma = 42.576 \cdot 10^6$ Hz/T and consequently the frequency of the RF field is approximately 64 MHz, 128 MHz, and 298 MHz for MR systems with a field strength of 1.5T, 3T, and 7T, respectively.

J.H.F. van Gemert and R.F. Remis are with the Circuits & Systems Group of the Electrical Engineering, Mathematics and Computer Science faculty of the Delft University of Technology.

W.M. Brink and A.G. Webb are with the C.J. Gorter Center of the Leiden University Medical Center.

Manuscript XX, 2018; revised XX, 2017.

To acquire high quality MR images the magnitude of the forward circularly polarized component of the RF magnetic field should be strong and uniform. In terms of the Cartesian components of the magnetic flux density phasor, this component is given by

$$B_1^+ = \frac{B_\mathrm{x} + \mathrm{j}B_\mathrm{y}}{2}, \tag{2}$$

where j is the imaginary unit. A high efficiency with respect to input power is desired, defined as $|B_1^+|/\sqrt{\mathrm{P_{in}}}$, to ensure minimal energy to be deposited in the subject and to enable a wider range of sequences to be ran within the peak power limitations of the system. However, the increase in RF frequency for higher field strengths leads to a shortening of the RF wavelength in tissue, leading to interference effects that reduce the uniformity of the $|B_1^+|$ distribution. Resulting areas of low transmit sensitivity translate into areas of low signal intensity and reduced contrast in the resulting MR images, limiting the image quality [2]-[6].

The RF uniformity can be improved by active or passive RF shimming techniques that tailor the B_1^+ field distribution. The active method uses transmit arrays and involves advanced additional hardware [7], [8]. Although many studies have been published on active RF shimming, complex issues of calculating the power deposited in the patient with variable transmit phases from the individual elements of the array have meant that this approach has not yet been used clinically, except for two-channel body coil shimming for clinical 3T systems. The alternative approach using passive RF shimming in the form of dielectric pads, on the other hand, is relatively cheap and easy to use. Typically, these dielectric pads are placed in the vicinity of the region of interest (ROI) and have a high relative permittivity up to 300 [9]. A properly designed pad, that is, a pad with the correct dimensions, constitution, and appropriate position, will generate a B_1^+ field perturbation that adds constructively to the total B_1^+ distribution and consequently on the acquired image [10]-[18].

Obtaining an optimal pad design is not straightforward, however, and the correct positioning of such a pad is in general not known. Therefore, it involves a multitude of design parameters that need to be optimized. To obtain the optimal pad design for a specific case it is common practice to perform a parametric design study by evaluating the RF response of a large number of pad realizations with different dimensions, locations, and constitution. As the parameter space is very

large, and it involves a very large computational domain encompassing a heterogeneous body model and coil model, such trial-and-error approaches are in general very time consuming, involve many human interactions, can only address a limited set of parameters, and often are not guided by any enforced optimality principle. Furthermore, the optimal design may vary with variations in the size and shape of the subject's anatomy. In addition, when the transmit antennas in a certain configuration differ from another configuration, or when the magnitude of the B_0 differs, a new pad should be designed. As each application requires a dedicated pad, it is beneficial to have a fast, structured, and efficient method for designing dielectric pads.

In our previous work [13], [19], we proposed a scattering formalism to significantly reduce the computation time for B_1^+ field evaluations of dielectric pads. The general idea in this approach is to first identify a spatial domain outside the body where the dielectric pad could be located, referred to as the "design domain." The design domain is typically very small compared with the total computational domain, which allows efficient evaluation of the B_1^+ field distribution from a specific pad that is confined within this domain. Although this method is efficient for evaluating single pad realizations, it does not yield sufficient acceleration to address the design problem efficiently and systematically.

In this paper, we extend our previous work by reducing the dimensionality of the model and subsequently using this reduced model in an optimization method to design dielectric pads. First, we exploit the fact that the constitution of practical pads does not vary on a voxel-by-voxel scale and it is therefore not necessary to allow for voxelwise variation in the constitution and size of a pad. The design domain is therefore subdivided into large nonoverlapping subdomains. Hereafter, we describe a pad in terms of parameters that control its dimensions, position, and constitution Subsequently, this parametric field representation is reduced via a projection based model order reduction technique [20] which decreases the computation time for single pad evaluations further. We can now design pads very efficiently by minimizing a cost functional that measures the discrepancy between the reduced-order field representations and a desired B_1^+ field distribution. Finally, we demonstrate the effectiveness of our approach by designing a dielectric pad for imaging the cerebellum at 7T, which is a difficult region to scan with commonly available RF head coils [21]-[29]. A parametric pad design study of the cerebellum has not been shown before, and therefore we use such a study here to demonstrate the method.

II. Methods

Spatially discretizing Maxwell's equations on a standard staggered finite-difference grid (Yee grid, [33]) and applying the above mentioned scattering formalism, the discretized B_1^+ field can be written as [19]

$$\mathsf{B}_1^+(\mathsf{c}) = \mathsf{B}_1^{+;\text{no pad}} + \mathsf{G}^{B_1^+\mathrm{J}} \left[\mathsf{I}_P - \mathsf{X}_{\text{pad}}(\mathsf{c})\mathsf{G}^{\mathrm{EJ}}\right]^{-1} \mathsf{X}_{\text{pad}}(\mathsf{c})\mathsf{E}^{\text{no pad}}, \quad (3)$$

where $\mathsf{B}_1^{+;\text{no pad}}$ represents the simulated and discretized B_1^+ field without a dielectric pad, whereas the second term on the right-hand side is the scattered B_1^+ field due to a dielectric pad, $\mathsf{E}^{\text{no pad}}$ is the simulated and discretized background electric field strength in the pad design domain when no pad is present and, finally, $\mathsf{X}_{\text{pad}} = \text{diag}(\mathsf{c})$ is a diagonal contrast matrix that is used to define the dielectric pad (dimensions, location, and constitution) within the pad design domain. Its diagonal elements are defined by the P-by-1 vector $\mathsf{c} = [c_1, c_2, ..., c_P]^T$ with

$$c_p = \sigma(\mathbf{r}_{k_p}) + \mathrm{j}\omega\varepsilon_0[\varepsilon_{\mathrm{r}}(\mathbf{r}_{k_p}) - 1] \quad (4)$$

for $p = 1, 2, ..., P$ and where $\sigma(\mathbf{r}_k)$ and $\varepsilon_{\mathrm{r}}(\mathbf{r}_k)$ are the conductivity and relative permittivity at grid edge location $\mathbf{r}_k$ with $k \in \mathcal{P} = \{k_1, k_2, \ldots, k_P\}$. Here, $\mathcal{P}$ is the index set of the pad design domain and P the total number of grid edges belonging to this domain. G^{EJ} and $\mathsf{G}^{B_1^+\mathrm{J}}$ are the discretized Green's tensors of the inhomogeneous background that map electric currents to the electric field strength and B_1^+ field, respectively. The former is used to compute the electric current distribution in the pad design domain, whereas the latter maps this electric current distribution to the B_1^+ field in the ROI. These discretized tensors are constructed one column at a time by computing the field responses due to Hertzian dipoles located at primary edges that belong to the pad design domain. Since these tensors are independent of the dielectric pad, we only have to compute them once and we store the computed field responses in what we call the Full Order Library (FOL). Having this library available, the scattered field due to any dielectric pad located within the pad design domain can now be efficiently computed, since for each realization only a system of order $P \ll N$ has to be solved, with N being the number of grid edges in the total computational domain.

A. Constructing Dielectric Subdomains

In the above scattering formalism, the conductivity and relative permittivity can vary on a voxel-by-voxel scale within the pad design domain. Allowing for this many degrees of freedom is not needed, however, since pads that vary in their constitution on a voxel scale are never realized in practice. We therefore reduce the number of unknowns by first subdividing the design domain into subdomains with constant material parameters, and then describing the dielectric pad as a collection of these subdomains. Taking the diagonal matrix representation $\mathsf{X}_{\text{pad}} = \text{diag}(\mathsf{c})$ as a starting point, we form dielectric subdomains by specifying the same material properties at grid edges that belong to a certain subdomain. Consequently, with a pad domain that is subdivided into D nonoverlapping homogeneous subdomains, the contrast matrix can be written as

$$\mathsf{X}_{\text{pad}} = \sum_{i=1}^{D} c_i \mathsf{X}_{\text{pad};i}, \quad (5)$$

where c_i is the contrast of the ith subdomain and $\mathsf{X}_{\text{pad};i}$ is its diagonal P-by-P support matrix. Substitution of this

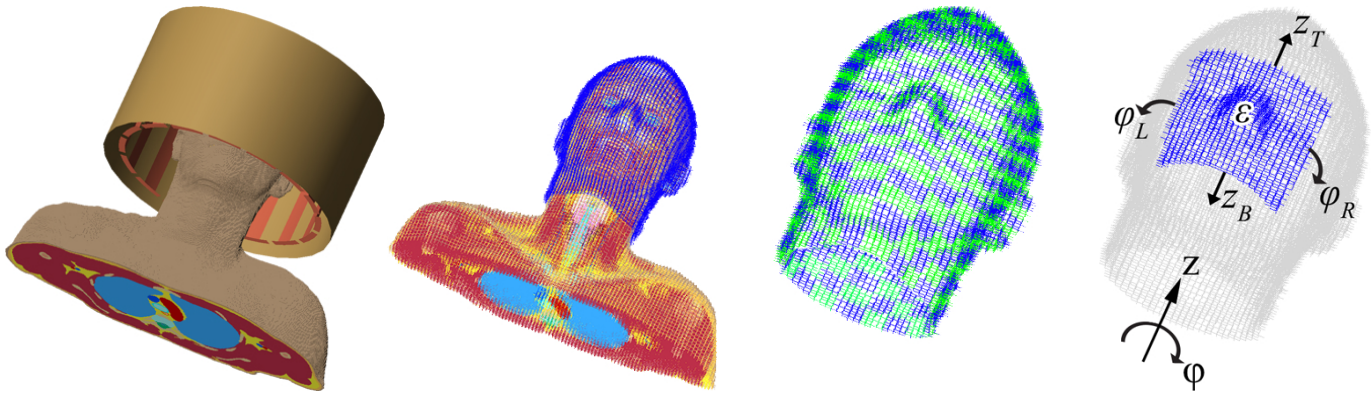

(a) (b) (c) (d)

Fig. 1. Head and shoulders of the male body model Duke, head coil, and shield used for enhanced imaging of the cerebellum (a). The pad design domain defined all around the head model (b). Pad design domain subdivided into subdomains (c). Illustration of the pad design parameters (d).

decomposition in Eq. (3) gives

$$\mathsf{B}_1^+ = \mathsf{B}_1^{+;\text{no pad}} + \mathsf{G}^{B_1^+\mathrm{J}} \left[\mathsf{I}_P - \sum_{i=1}^{D} c_i \mathsf{G}_i^{\mathrm{EJ}} \right]^{-1} \sum_{i=1}^{D} c_i \mathsf{X}_{\text{pad};i} \mathsf{E}^{\text{no pad}}, \tag{6}$$

where we have introduced the P-by-P Greens tensor matrix that corresponds to the ith subdomain as $\mathsf{G}_i^{\mathrm{EJ}} = \mathsf{X}_{\text{pad};i}\mathsf{G}^{\mathrm{EJ}}$ for $i = 1, 2, ..., D$. Figure 1c shows a subdivision of the pad design domain of Figure 1b into subdomains. The contrast within each subdomain is constant.

B. Pad Parametrization

The majority of dielectric pads that are realized in practice have a rectangular shape and are homogeneous. To take this into account in our subdomain formalism, we introduce a set of pad design parameters that fully describe such practical pads. Specifically, in cylindrical coordinates (with the z-axis parallel to the bore of the MRI scanner), the z-coordinate of the bottom and top edge of a pad are denoted by z_{B} and z_{T}, respectively, while the edges of the pad in the azimuthal direction have φ_{L} and φ_{R} as angular coordinates (see Figure 1d). Furthermore, since the pads are typically homogeneous, the conductivity σ and relative permittivity ε_{r} of the pad are constant. In our implementation, we fix the conductivity of the pad, since the B_1^+ field is generally much more sensitive to variations in the permittivity. For simplicity, we do not vary the thickness of the pad either, but we stress that, if desired, thickness variations can be included as well.

To summarize, the parameters that we use to describe a pad within the pad design domain are the coordinates z_{B}, z_{T}, φ_{L}, φ_{R}, and the relative permittivity ε_{r} of the pad as shown in Figure 1d. To indicate that the B_1^+ field depends on these parameters, we write $\mathsf{B}_1^+ = \mathsf{B}_1^+(\mathsf{p})$, where p is the parameter vector

$$\mathsf{p} = \left[z_{\mathrm{B}}, z_{\mathrm{T}}, \phi_{\mathrm{L}}, \phi_{\mathrm{R}}, \varepsilon_{\mathrm{r}} \right]^T. \tag{7}$$

Finally, to enforce a rectangular shape for a dielectric pad, we use an approximation of the Heaviside step function given by

$$\tilde{u}(x,k) = \frac{1}{1+\exp(-2kx)}, \tag{8}$$

where k determines the smoothness (i.e. $k \to \infty$ gives the true Heaviside function) and x is a normalized coordinate. By using these approximate step functions for each of the cylindrical coordinates z and φ separately, we are able to impose a rectangular shape for the pads into our subdomain formalism. In particular, the pad parametrization can be included through the parameter dependent contrast functions

$$\begin{aligned} \mathsf{f}_i(\mathsf{p}) = {} & [\sigma + \mathrm{j}\omega\varepsilon_0(\varepsilon_{\mathrm{r}} - 1)] \cdot \\ & \left\{ \tilde{u}\left[\frac{1}{z_\ell}(z_i - z_{\mathrm{T}}), k\right] - \tilde{u}\left[\frac{1}{z_\ell}(z_i - z_{\mathrm{B}}), k\right] \right\} \cdot \\ & \left\{ \tilde{u}\left[\frac{1}{2\pi}(\varphi_i - \varphi_{\mathrm{L}}), k\right] - \tilde{u}\left[\frac{1}{2\pi}(\varphi_i - \varphi_{\mathrm{R}}), k\right] + \right. \\ & \tilde{u}\left[\frac{1}{2\pi}(\varphi_i - \varphi_{\mathrm{L}} + 2\pi), k\right] - \tilde{u}\left[\frac{1}{2\pi}(\varphi_i - \varphi_{\mathrm{R}} + 2\pi), k\right] + \\ & \left. \tilde{u}\left[\frac{1}{2\pi}(\varphi_i - \varphi_{\mathrm{L}} - 2\pi), k\right] - \tilde{u}\left[\frac{1}{2\pi}(\varphi_i - \varphi_{\mathrm{R}} - 2\pi), k\right] \right\}. \end{aligned} \tag{9}$$

where z_i and φ_i are the coordinates of the midpoint of the ith subdomain and z_ℓ is the length of the pad design domain, as illustrated in Fig. 2. The first term on the right-hand side of Eq. (9) determines the shape in the z-direction, whereas the other three terms determine the shape in the φ-direction. The third and fourth term are two shifted versions of the second term (over 2π and -2π, respectively) to enforce continuity. Finally, the arguments of the approximated Heaviside functions are normalized such that the smoothness parameter k has the same influence on all normalized coordinates.

With the introduction of the contrast functions of Eq. (9), the parameter dependent expression for the B_1^+ field is given by

$$\mathsf{B}_1^+(\mathsf{p}) = \mathsf{B}_1^{+;\text{no pad}} + \mathsf{G}^{B_1^+\mathrm{J}} \left[\mathsf{I}_P - \sum_{i=1}^{D} \mathsf{f}_i(\mathsf{p}) \mathsf{G}_i^{\mathrm{EJ}} \right]^{-1} \sum_{i=1}^{D} \mathsf{f}_i(\mathsf{p}) \mathsf{X}_{\text{pad};i} \mathsf{E}^{\text{no pad}}. \tag{10}$$

This parameterized field expression serves as a starting point in the projection based model reduction technique discussed in the next section.

C. Projection Based Model Reduction

By introducing the electric current state vector as

$$\mathsf{j}(\mathsf{p}) = \left[\mathsf{I}_P - \sum_{i=1}^{D} \mathsf{f}_i(\mathsf{p})\mathsf{G}_i^{\mathrm{EJ}}\right]^{-1} \sum_{i=1}^{D} \mathsf{f}_i(\mathsf{p})\mathsf{X}_{\mathrm{pad};i}\mathsf{E}^{\text{no pad}}, \quad (11)$$

representing the conduction currents and the displacements currents in the pad design domain, the B_1^+ field of Eq. (10) can be written as

$$\mathsf{B}_1^+(\mathsf{p}) = \mathsf{B}_1^{+;\text{no pad}} + \mathsf{G}^{B_1^+\mathrm{J}}\mathsf{j}(\mathsf{p}). \quad (12)$$

This equation provides a direct relationship between the B_1^+ field within the region of interest and induced electric currents with their support in the pad design domain. Obviously, different pad realizations produce different induced currents densities resulting in different B_1^+ field patterns within a region of interest. According to Eq. (11), to obtain the current vector $\mathsf{j}(\mathsf{p})$ for a certain pad relatization as described by the parameter vector p, a system of order P has to be solved. Even though this order is much smaller than the total order N of the system, a further reduction may be achieved by representing a general current vector $\mathsf{j}(\mathsf{p})$ in terms of a reduced basis consisting of $r \ll P$ basis vectors. If such a reduced basis can be found, then evaluating specific pad realizations would involve solving a system of order r instead of order P. This is particularly beneficial in a pad optimization framework (see Section II-D), since it allows us to efficiently compute B_1^+ fields due to pads with different pad design parameters.

To find a reduced order basis for the induced current densities, we follow a Projection Based Model Reduction approach as outlined in [20], for example. Specifically, for a given set of different pad design vectors p_1, p_2, ..., p_S, we first compute the corresponding induced current densities $\mathsf{j}(\mathsf{p}_1)$, $\mathsf{j}(\mathsf{p}_2)$, ...,$\mathsf{j}(\mathsf{p}_S)$ and store these distributions as columns in a snapshot matrix S, i.e.

$$\mathsf{S} = [\mathsf{j}_1(\mathsf{p}_1) \ldots \mathsf{j}_S(\mathsf{p}_S)], \quad (13)$$

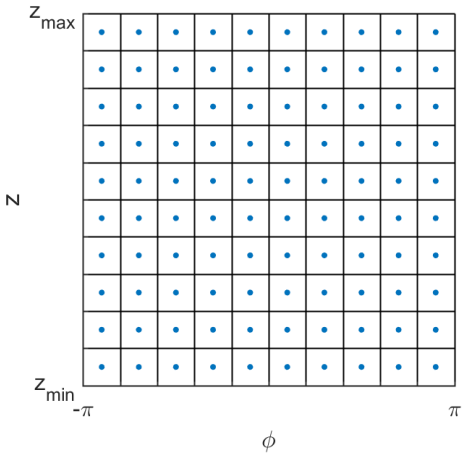

Fig. 2. Subdomains of the the pad design domain. The coordinates of the subdomain $\{\varphi_i, z_i\}$ refer to the midpoint of each subdomain indicated by the dot. The length of the pad design domain is z_ℓ, i.e. $z_\ell = |z_{\max} - z_{\min}|$.

where $S \geq 1$ is the number of snapshots. Subsequently, we compute the thin singular value decomposition of the snapshot matrix. This decomposition is given by

$$\mathsf{S} = \mathsf{U}\Sigma\mathsf{V}^H, \quad (14)$$

where the columns of U and V are the left and right singular vectors of the snapshot matrix, while Σ is a diagonal matrix with positive decreasing singular values on its diagonal, i.e. $\sigma_i \geq \sigma_{i+1}$. To remove possible redundancy among the computed currents $\mathsf{j}(\mathsf{p}_i)$, we now take the r most significant left-singular vectors corresponding to the r largest singular values as basis vectors to describe an arbitrary current distribution $\mathsf{j}(\mathsf{p})$. In other words, we approximate the current distribution by the reduced-order model

$$\mathsf{j}_r(\mathsf{p}) = \alpha_1(\mathsf{p})\mathsf{u}_1 + \alpha_2(\mathsf{p})\mathsf{u}_2 + \ldots + \alpha_r(\mathsf{p})\mathsf{u}_r = \mathsf{U}_r\mathsf{a}_r(\mathsf{p}), \quad (15)$$

where the basis matrix U_r has the column partitioning $\mathsf{U}_r = [\mathsf{u}_1, \mathsf{u}_2, ..., \mathsf{u}_r]$ and $\mathsf{a}_r(\mathsf{p}) = [\alpha_1(\mathsf{p}), ..., \alpha_r(\mathsf{p})]^T$ is the vector of expansion coefficients. To find these coefficients, we require that the residual of the reduced-order model

$$\mathsf{r} = \sum_{i=1}^{D} \mathsf{f}_i(\mathsf{p})\mathsf{X}_{\mathrm{pad};i}\mathsf{e}^{\text{no pad}} - \left[\mathsf{I}_P - \sum_{i=1}^{D} \mathsf{f}_i(\mathsf{p})\mathsf{G}_i^{\mathrm{EJ}}\right] \mathsf{U}_r\mathsf{a}_r(\mathsf{p}) \quad (16)$$

is orthogonal to the basis vectors u_i, $i = 1, 2, ..., r$, that is, the expansion coefficients are found from the Galerkin condition $\mathsf{U}_r^H\mathsf{r} = 0$ as

$$\mathsf{a}_r(\mathsf{p}) = \left[\mathsf{I}_r - \sum_{i=1}^{D} \mathsf{f}_i(\mathsf{p})\mathsf{G}_i^{\mathrm{EJ};r}\right]^{-1} \sum_{i=1}^{D} \mathsf{f}_i(\mathsf{p})\mathsf{X}_{\mathrm{pad};i}^r\mathsf{E}^{\text{no pad}}, \quad (17)$$

where I_r is the identity matrix of order r and where we have introduced the reduced matrices $\mathsf{G}_i^{\mathrm{EJ};r} = \mathsf{U}_r^H\mathsf{G}_i^{\mathrm{EJ}}\mathsf{U}_r$ and $\mathsf{X}_{\mathrm{pad};i}^r = \mathsf{U}_r^H\mathsf{X}_{\mathrm{pad};i}$. It should be noted that, in order to compute the expansion coefficients, a system of order r needs to be solved instead of a system of order P as in Eq. (10). Finally, substituting the reduced-order model for the currents in Eq. (12), we arrive at the reduced-order model for the B_1^+ field as

$$\mathsf{B}_1^{+;r}(\mathsf{p}) = \mathsf{B}_1^{+;\text{no pad}} + \mathsf{G}^{B_1^+\mathrm{J};r}\mathsf{a}_r(\mathsf{p}), \quad (18)$$

where $\mathsf{G}^{B_1^+\mathrm{J};r} = \mathsf{G}^{B_1^+\mathrm{J}}\mathsf{U}_r$ maps the expansion vector of the currents as given by Eq. (17) to the B_1^+ field. The reduced matrices $\mathsf{G}_i^{\mathrm{EJ};r}$, $\mathsf{X}_{\mathrm{pad};i}^r$, and $\mathsf{G}^{B_1^+\mathrm{J};r}$ constitute the reduced order library (ROL).

D. Pad design for cerebellum imaging

Having the parametrized reduced-order model for the B_1^+ field as given by Eq. (18), allows the design of an optimal pad for a certain ROI within the human body. As an illustrative example, we focus on imaging of the cerebellum at 7T, but we stress that the approach can equally be applied to other parts of the human body as well.

To find a pad design for which the amplitude of the B_1^+ field is as uniform as possible within the ROI, we minimize the cost function

$$C(\mathsf{p}) = \frac{1}{2}\frac{\|\mathsf{B}_1^{+;r}(\mathsf{p}) - \mathsf{B}_1^{+;\text{desired}}\|_2^2}{\|\mathsf{B}_1^{+;\text{desired}}\|_2^2}, \quad (19)$$

over all feasible pad parameter vectors p, where $\mathsf{B}_1^{+;r}(\mathsf{p})$ and $\mathsf{B}_1^{+;\text{desired}}$ are the modeled and desired B_1^+ fields within the ROI, respectively. Since we only prescribe the amplitude of the desired B_1^+ field throughout the ROI (1 μT, for example) we follow [34] and take

$$\mathsf{B}_1^{+;\text{desired}} = b \exp\left[\mathrm{j}\angle \mathsf{B}_1^{+;r}(\mathsf{p})\right], \tag{20}$$

for the desired complex B_1^+ field, where b is the prescribed amplitude. In other words, the phase of the desired field is set equal to the phase of the current B_1^+ field.

Since the cost functional of Eq. (19) defines a nonlinear least squares problem, we minimize $C(\mathsf{p})$ using the standard Levenberg-Marquardt algorithm [35]. This minimization procedure should take place over feasible pad parameter vectors, i.e. describing physically realizable dielectric pads. We include this requirement by imposing the constraints $\varepsilon_\mathrm{r} \geq 1$, $|\varphi_\mathrm{R} - \varphi_\mathrm{L}| \geq \ell$, $|z_\mathrm{T} - z_\mathrm{B}| \geq w$, and $z_\mathrm{T} \leq d$. The first constraint is implemented by writing the relative permittivity as $\varepsilon_\mathrm{r} = 1 + \epsilon^2$ and taking ϵ as an optimization parameter. The second and third constraint are implemented by setting the length and width of the pad to the minimum length ℓ and minimum width w, respectively, whenever a length or width is found that is smaller than these prescribed minima. The last constraint is included so that no pads will be positioned at the top of the head, since the contrast functions $f_i(\mathsf{p})$ degenerate into triangles in this region. The triangles result since all subdomains in this region are bend to the same center point on top of the head. We implement this constraint by setting z_T equal to its permitted value d whenever we encounter a z_T for which the fourth constraint is not satisfied. Finally, we note that since the reduced-order model for the B_1^+ field is used to describe the B_1^+ field, only systems of order r need to be solved to determine the elements of the Jacobian, since the pad parameters occur in the r expansion coefficients $\alpha_i(\mathsf{p})$ only.

III. Implementation and Results

To illustrate the performance of our dielectric pad design procedure, we have divided this section into three parts. First, we construct an FOL without any model reduction using the technique proposed in our previous work [19]. We subsequently reduce this library using the parametric reduced-order modeling techniques described in Section II. These reduction techniques produce an ROL and we demonstrate the accuracy of the ROL by comparing B_1^+ field maps computed with the FOL with B_1^+ maps computed using the ROL. Finally, in the third part, we design a dielectric pad for cerebellum imaging, after which we validate our design using an MR measurement.

A. Creating the Full Order Library

The configuration that is used for simulations is depicted in Fig. 1a and consists of the head and shoulders of the male body model "Duke" from the Virtual Family dataset [36], and a shielded 16-rung high-pass birdcage coil. The coil has an inner radius of 15 cm and outer radius of 18 cm and operates in quadrature mode at a frequency of 298 MHz which corresponds to the ^{1}H Larmor frequency at 7T. The birdcage is tuned using 6.7 pF capacitors and driven by two current sources. The resulting electromagnetic fields from this loaded coil have been normalized to 1 W input power. These fields are computed using XFdtd software (v.7.5.0.3,Remcom State College, PA, USA) with a voxel size of 5 mm^3. Computations are performed on a Windows 64-bit machine with an Intel Xeon CPU X5660 @ 2.80 GHz (dual core) with 48 GB internal memory and two NVIDIA Tesla K40c GPU's.

The pad design domain is defined as a continuous layer covering the head with a thickness of 1 cm (to fit inside the close-fitting 32-channel receive array) as depicted in Fig. 1b. This domain consists of about $P = 27,000$ FDTD primal grid edges, i.e. edges where the material of a dielectric pad can be defined. As outlined above, for each grid edge in the pad design domain we perform a single simulation, after which the FOL is constructed. Constructing this library took approximately 48 hrs and results in 30 GB of data. We note that, once it is generated, any pad within the pad domain can be modeled using this library.

B. Creating the Reduced Order Library

To compress the library, we now divide the pad design domain into $D = 400$ subdomains with 20 subdivisions in the z-direction and 20 subdivisions in the φ-direction as illustrated in Fig. 1d. The average resolution of one subdomain is about $3 \times 1.2 \times 1$ cm^3 ($\varphi \times z \times$ thickness).

Subsequently, the snapshot matrix S of Eq. (13) is constructed by performing $S = 2000$ simulations in Remcom XFdtd for different pad realizations described by the parameters of Eq. (7). For each pad, the pad parameters are chosen randomly (using the function *rand* in Matlab) and such that the pads have a minimum width of $w = 3$ cm, a minimum length of $\ell = \pi/5$, and a top edge z-coordinate that satisfies $z_\mathrm{T} < 5$ cm. These parameters constraints were also used in the Levenberg-Marquardt algorithm during the pad design stage (see below). Moreover, all randomly generated pads have a relative permittivity smaller than 500, since pads with a higher relative permittivity are difficult to realize in practice. In each simulation, the electric current density in the pad design domain is computed and stored as a column in the snapshot matrix S.

Having the snapshot matrix available, we compute its SVD. We select the first $r = 500$ left singular vectors as expansion vectors in our reduced-order model ($\sigma_{500} = 0.0044$). As a rule,

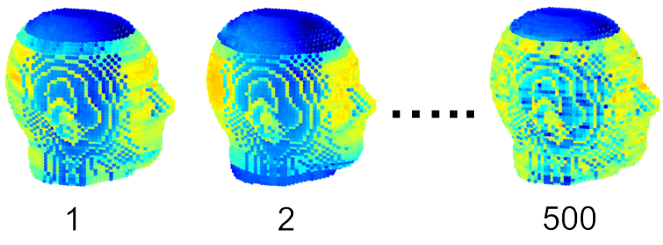

Fig. 3. Illustration of the first, second, and 500$^{\text{th}}$ left singular vector of the snapshot matrix are shown. These vectors represent electric currents in the pad design domain.

we generally include all left singular vectors in our reduced order basis for which the corresponding normalized singular values are larger than 0.004. Three of these singular vectors are shown in Fig. 3, which physically represent electric currents in the pad design domain.

With the 500 most dominant singular vectors at our disposal, we now form the reduced matrices $\mathsf{G}_i^{\mathrm{EJ};r} = \mathsf{U}_r^H \mathsf{G}_i^{\mathrm{EJ}} \mathsf{U}_r$, $\mathsf{X}_{\mathrm{pad};i}^r = \mathsf{U}_r^H \mathsf{X}_{\mathrm{pad};i}$, and $\mathsf{G}^{B_1^+\mathrm{J};r} = \mathsf{G}^{B_1^+\mathrm{J}} \mathsf{U}_r$. As mentioned above, these matrices constitute the ROL and this library requires significantly less memory than the FOL. To be specific, for the problem considered here, disk storage for the ROL is approximately 1 GB, which amounts to a storage reduction factor of 30 compared with the FOL storage requirement. Moreover, to compute the B_1^+ field for different pad realizations, systems of order $P = 27,000$ need to be solved when using the FOL, while reduced systems of order $r = 500$ need to be solved when using the ROL. In particular, for the cerebellum imaging problem considered here, a B_1^+ field evaluation for a single pad realization takes about 90 seconds on the computer system system mentioned above (using the GMRES iterative solver [37] with a tolerance of 10^{-6}) when the FOL is used, while the computation time for evaluating the reduced-order model is approximately 0.35 seconds, which amounts to a speed up factor of 260. Finally, in Fig. 5 we show the absolute error for three different pad realizations of the reduced-order models at cross-sections where this error is maximum (the maximum being defined over the complete head and shoulder model). We observe that the reduced-order models are in good overall agreement with the B_1^+ field computed using XFdtd and maxima in the absolute error essentially occur only at the outer periphery very close to the dielectric pads. The reduced-order fields can therefore safely be used in the pad optimization stage to efficiently design a dielectric pad for cerebellum imaging.

C. Designing pads

Imaging the cerebellum at 7T has its difficulties due to the reduced RF homogeneity. At this particular ROI, there is a substantial drop-off in the sensitivity of the volume transmit coil that leads to poor image quality (see Fig. 7a and Fig. 7b). The simulated background B_1^+ field (i.e. without any pad) is shown in the left column of Fig. 6 for a coronal and transverse slice through the cerebellum. Clearly, we can see the reduced transmit sensitivity in the cerebellum ROI, which is outlined by the black line. Explicitly, the mean B_1^+ field in the ROI is $0.29\ \mu\mathrm{T}/\sqrt{\mathrm{W}}$ and the coefficient of variation $\mathrm{C_v}$ is 34%, i.e. the ratio of the standard deviation to the mean. Our aim is to optimize the B_1^+ field within this ROI using a dielectric pad, i.e. we aim at increasing the transmit sensitivity by designing a pad that yields a homogeneous high-intensity field.

Minimizing the cost functional from Eq. (19) results in optimizing both transmit efficiency and homogeneity of the B_1^+ field, but it does not address the balance between the two. Furthermore, the permittivity of the optimized pad is not restricted to a set a values, but can take any permittivity value. In practice, a wide range of relative permittivities can be fabricated, but only up to a maximum of 300 [9]. Therefore, to find the optimal pad that increases both transmit efficiency and homogeneity, and can be fabricated, we run the optimization algorithm multiple times for different desired field strengths, which can be done since our optimization algorithm is very efficient. To this end, the $\mathsf{B}_1^{+;\mathrm{desired}}$ field in the cost functional is initially set to the B_1^+ field per square root of input power that is produced by the birdcage transmit coil with no dielectric present. Repeatedly, we increase the desired field strength and optimize for the pad parameters after which we list the relative permittivity and the coefficient of variation $\mathrm{C_v}$ of the B_1^+ field in the cerebellum. The results are depicted in the graph of Fig. 4. Subsequently, the dielectric is selected that gave the best performance in terms of transmit efficiency and homogeneity, and leads to a flexible pad that can be fabricated. This corresponds to the optimization where the $\mathsf{B}_1^{+;\mathrm{desired}}$ field has been set to $0.48\ \mu\mathrm{T}/\sqrt{\mathrm{W}}$. We stress, that the trends of these curves are not known beforehand and a permittivity value that is too high can decrease both transmit efficiency and $\mathrm{C_v}$.

TABLE I
SENSITIVITY ANALYSIS OPTIMAL PAD

Pad	$\mathrm{C_v}$ (%)	Transmit efficiency ($\mu\mathrm{T}\sqrt{\mathrm{W}}$)
None	34	0.29
Optimal	14	0.48
Optimal ε_r increased by 10% to 325	13	0.50
Optimal ε_r decreased by 10% to 266	16	0.46
Optimal shifted vertically by 1.2 cm	20	0.44
Optimal shifted horizontally by 3 cm	17	0.47
Optimal width changed by $\pm$3 cm	17	0.47
Optimal length changed by $\pm$1.2 cm	20	0.44

For this particular optimization, the optimal pad has been found within 10 iterations, which takes about 30 seconds on the above mentioned computer system. The resulting pad has a relative permittivity of $\varepsilon_\mathrm{r} = 295$ and dimensions $32 \times 9.5 \times 1$ cm^3. The transmit efficiency has increased by 66% from $0.29\ \mu\mathrm{T}/\sqrt{\mathrm{W}}$ to $0.48\ \mu\mathrm{T}/\sqrt{\mathrm{W}}$ and the coefficient of variation of the B_1^+ in the cerebellum has decreased from 34% to 14%. We subsequently fabricated this pad using a mixture of barium titanate and deuterated water [9]. For the optimum dielectric pad we carry out a sensitivity analysis to investigate the possible decrease in optimality for near-optimal parameters, as this might occur when fabricating and positioning the pad in practice. The optimal parameters are perturbed and the resulting change in the coefficient of variation and the transmit efficiency are listed, as shown in Table I. This table is acquired in 3.5 seconds as forward simulations are evaluated quickly. In the worst-case scenario the $\mathrm{C_v}$ increases to 20% and the transmit efficiency reduces to $0.44\ \mu\mathrm{T}/\sqrt{\mathrm{W}}$ implying that the designed pad is not very sensitive to small changes.

Additionally, we investigate how this specific dielectric pad performs for a smaller female head model. To this end we replace the body model Duke in Remcom XFdtd by the female version Ella and run a simulation without dielectric pad and one with the previously-determined optimal dielectric

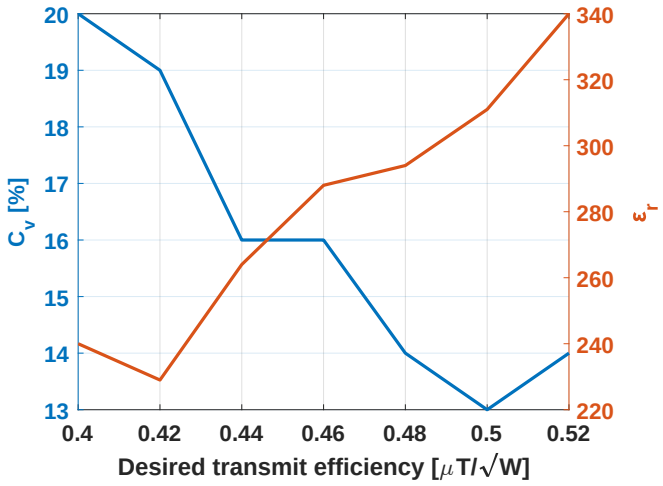

Fig. 4. The cost functional from Eq. (19) is optimized for different desired transmit efficiency's. The resulting coefficient of variation is shown on the left axis and the required permittivity on the right axis.

pad. Similar performance metrics were obtained as compared to those of the male head model. Specifically, a transmit efficiency gain of 64%, from $0.32\ \mu\mathrm{T}/\sqrt{\mathrm{W}}$ to $0.53\ \mu\mathrm{T}/\sqrt{\mathrm{W}}$, and the $\mathrm{C_v}$ decreases from 27% to 17%.

To confirm our findings with actual measurements T1-weighted and T2-weighted scans were acquired with and without the dielectric pad, as shown in Fig. 7c and Fig. 7d, respectively. The T1-weighted scans are obtained with a 3D Turbo Field Echo sequence with a FOV of $256 \times 256 \times 174.4$ mm^3 and an isometric resolution of 0.8 mm^3. The T2-weighted scans are acquired with a turbo spin echo sequence where a FOV is used of $107 \times 240 \times 198$ mm^3 and an in-plane resolution of 0.8×0.66 mm^2. The effect of the dielectric pad is clearly visible and increases the contrast and signal intensity in the cerebellum, improving the visibility of structural details, thereby confirming that the pad designed with our optimization technique is able to significantly improve the quality of MR images.

IV. Discussion and Conclusions

In this work we have presented a fast and efficient method for designing dielectric pads. The scattered field model presented in [19] was taken as a starting point, and we showed that the order of this model can be reduced to a great extent by employing a projection based model order reduction technique, which can subsequently be used in an optimization method. The scattered field models of [19] with an order of approximately 27,000 were successfully reduced to a system of order 500, thereby reducing the model order by a factor of 54. Having the reduced-order models available, B_1^+ field responses can be computed in a fraction of a second for each pad realization at the price of a negligible loss in accuracy.

The design of dielectric pads has been posed as an optimization problem in which a cost functional that measures the discrepancy between the modeled and desired B_1^+ field distribution is minimized over feasible pad parameters values, i.e. dimensions, location, and constitution. This optimization problem can be solved very efficiently, since the modeled field approximations in the cost function are of reduced-order. The optimization has been successfully applied to MR cerebellum imaging reducing the coefficient of variation by a factor 2.4. The resulting optimal pad has been fabricated and its performance was verified in an MR imaging experiment.

The optimization results from Fig. 6 show that the $\mathrm{C_v}$ and the transmit efficiency improve for every iteration. The dielectric from the third iteration, for example, improved the transmit efficiency already by 35%, but is still far from the optimal dielectric. This enforces the need for a rigorous optimization approach as shown in this work.

The dielectric pad might couple to the birdcage coil when the permittivity value is high and/or the distance from the coil is small. This coupling is taken into account in the current work since the library is constructed with a tuned birdcage coil present in the background. However, in the rare case that the birdcage should be retuned, a new library should be constructed. In future work, we investigate whether we could combine the method with co-simulation techniques to retune the coil without constructing a new library [40].

In the design process of this work, single dielectric pads have been considered that are homogeneous and have a simple geometry. A second dielectric pad can be included in the model as well, as this is often required in practical applications [10], [14], [15], [18], [38], [39]. However, the design could be much more sophisticated. For example, more complicated dielectric structures such as pre-fractal pads add several degrees of freedom to the design process [41], hence, increasing the complexity of the design problem. The design problem becomes even more computationally challenging when optimizing multi-element dielectric pads for multi-element RF transmit and receive coil arrays, in which increasingly dielectric materials are incorporated [42]. As the coupling between the dielectric and the coils is taken into account, one could think of optimizing for SNR, the g-factor for parallel imaging, or the receive sensitivities of the individual coil elements. Therefore, an efficient way of designing these pads as presented here becomes even more relevant.

In this current work, we created the snapshot matrix by simulating a large number of random pad realizations confined to the pad design domain. Since we used the method to optimize a pad for the cerebellum specifically, it would have also sufficed to reduce the random pad realizations to a domain that is more closely related to the extent of the ROI, hence reducing the size of the ROL even further. We stress, however, that by considering the entire design domain we have obtained a reduced-order model that is more generic and application independent. The method may still benefit from a more structured approach, nonetheless, e.g. by using a greedy algorithm that determines the next snapshot on the basis of maximum error reduction [20]. However, this requires an explicit expression for the projection error which needs further investigation.

Finally, two-sided reduction techniques can further speed up the design procedure. In the present work, reduced-order models for the induced currents in the pad design domain have

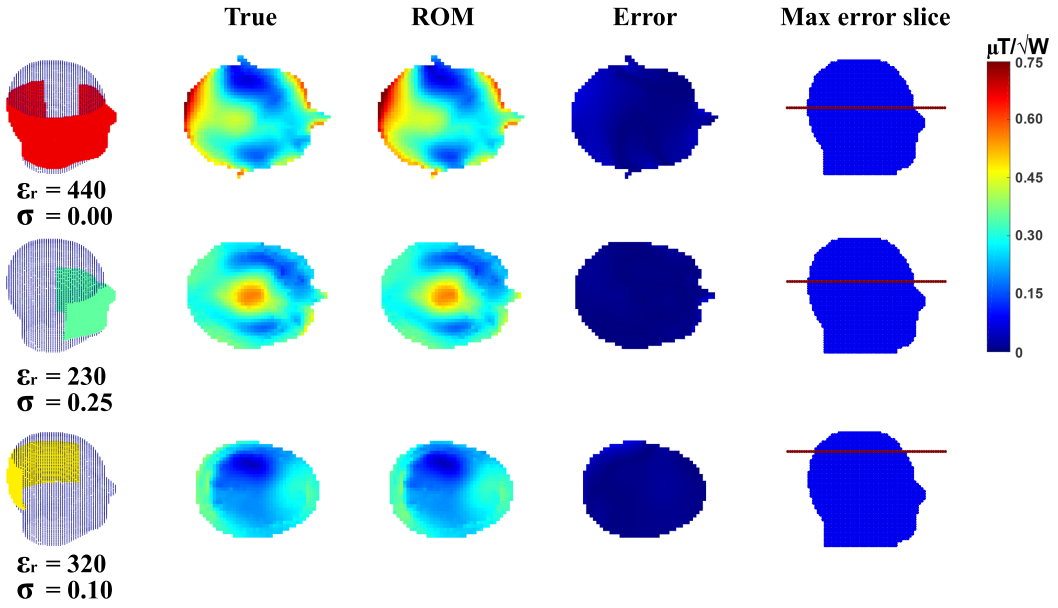

Fig. 5. Comparison of the transmit fields for three pad realizations with different material properties. The transverse slices where the maximum absolute B_1^+ errors occur are depicted. The absolute error in the third column is shown in the same color scale.

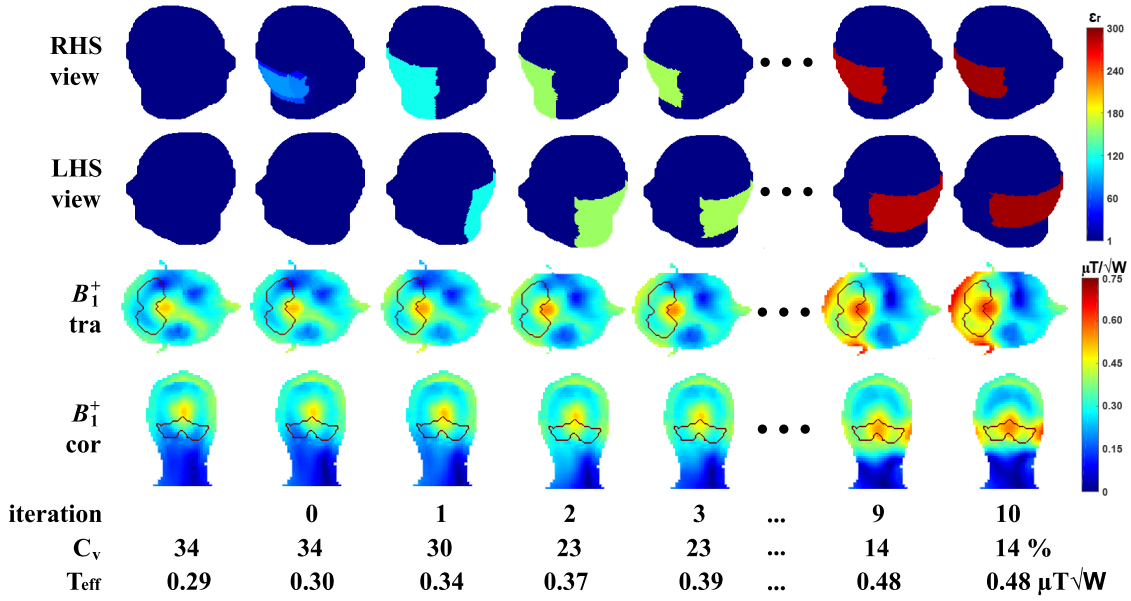

Fig. 6. Intermediate optimization results are shown. The first and second row illustrate the right and left hand side view of the head where the pad is formed. The third and fourth row depict the B_1^+ transmit fields for the transverse and coronal slice, respectively. The cerebellum is outlined, and in this ROI the signal intensity is low. The columns show a few of the iterations of the optimization method. After 10 iterations it has converged to an optimal dielectric pad. The figures shown at the bottom of the figure depict the intermediate coefficient of variation and transmit efficiency.

been constructed and the resulting B_1^+ fields are computed using the discretized electric current to B_1^+ Green's tensor (see Eq.(3)). Two-sided reduction techniques can also reduce the size of this operator, further reducing the complexity of the optimization potentially allowing for an even faster pad design procedure for any body part of interest.

ACKNOWLEDGMENT

The research reported in this paper is financially supported by the Dutch Technology Foundation (STW, project number 13375).

REFERENCES

[1] R. W. Brown, Y. N. Cheng, E. .M. Haacke, M. R. Thompson, and R. Venkatesan *Magnetic resonance imaging: physical principles and sequence design*, 1st Edition, John Wiley & Sons, 1999, p. 6.

[2] O. Dietrich, M. F. Reiser, and S. O. Schoenberg, "Artifacts in 3-T MRI: physical background and reduction strategies," *Eur J Radiol*, Vol. 65, No. 1, pp. 29 – 35, 2008.

[3] M. A. Bernstein, J. Huston, and H. A.Ward, "Imaging artefacts at 3.0 T," *J. Magn. Reson. Imaging*, Vol. 24, No. 4, pp. 735 – 746, 2006.

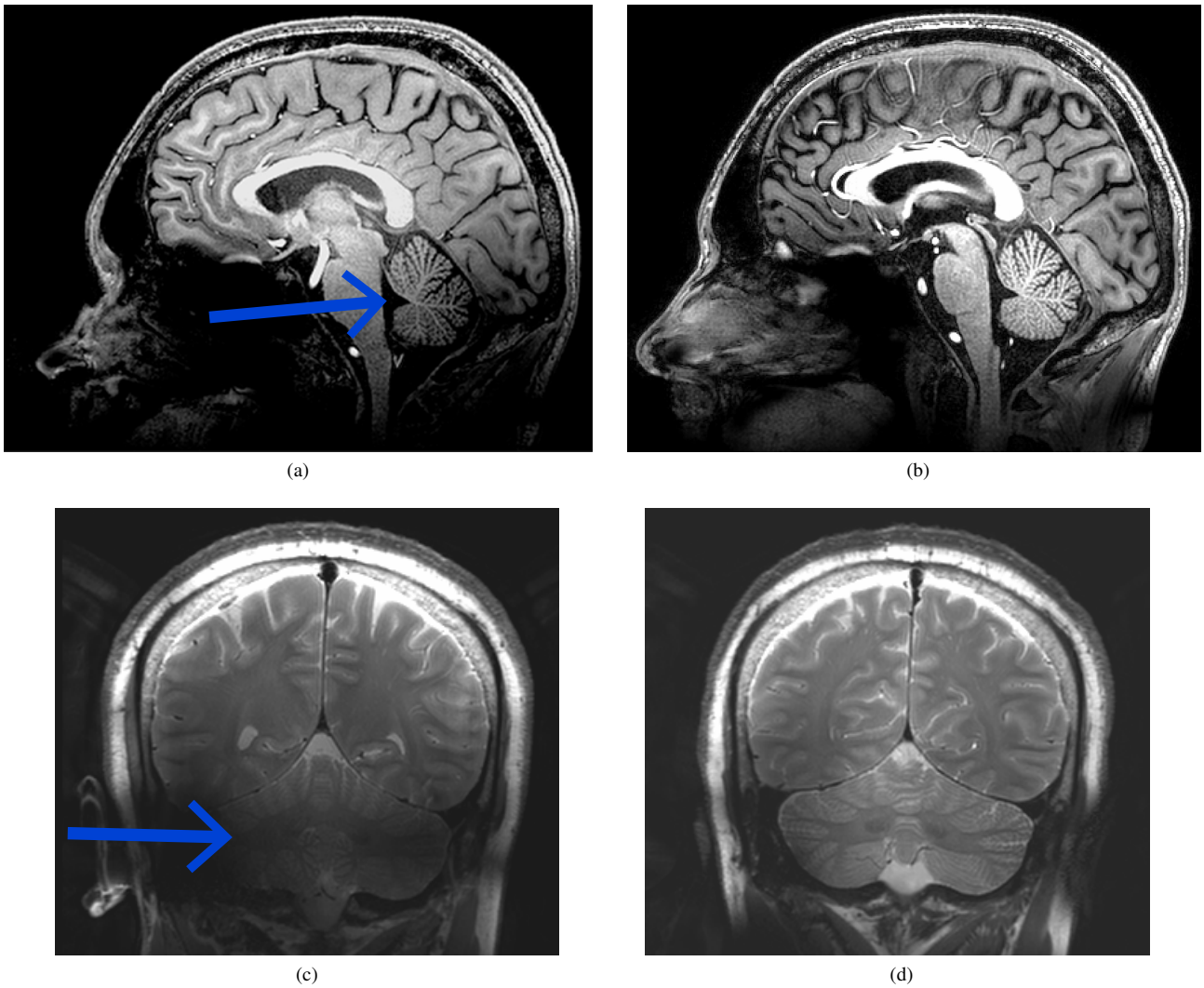

Fig. 7. T1 and T2 weighted head scans of the brain at 7T (298 MHz). Low contrast is encountered in the cerebellum due to non-uniformity in the B_1^+ transmit field indicated with the arrows. Scans have been obtained on a 7T Philips Achieva, where a quadrature head coil is used for transmission and a 32 channel receive array for reception. (a) A T1-weighted turbo field echo sequence was used with a TR of 5.5 ms. 218 slices were acquired with an isometric resolution of 0.8 mm^3 and a field-of-view of $256 \times 256 \times 174$ mm^3. The total scan time was 6 minutes. (b) A T2-weighted turbo spin echo sequence was used with a field-of-view of $107 \times 240 \times 198$ mm^3 and an in-plane resolution of 0.8×0.66 mm^2. The total scan time was 1.5 minutes for 17 slices. The left column shows the results without a dielectric pad, and the right column for an optimized dielectric pad. The pad has a relative permittivity of $\varepsilon_r = 295$, a conductivity of $\sigma = 0.2$ S/m, and dimensions $32 \times 9.5 \times 1$ cm^3. The optimized pad resolves the low signal intensities at the cerebellum.

[4] J. K. Chang and I. R. Kamel, "Abdominal imaging at 3T: challenges and solutions," *Appl. Radiol.*, Vol. 39, No. 10, pp. 22, 2010.

[5] K. Sung and K. S. Nayak, "Measurement and characterization of RF nonuniformity over the heart at 3T using body coil transmission," *J. Magn. Reson. Imaging*, Vol. 27, No. 3, pp. 643 – 648, 2008.

[6] J. T. Vaughan, M. Garwood, C. M. Collins, W. Liu, L. DelaBarre, G. Adriany, P. Andersen, H. Merkle, R. Goebel, M. B. Smith, and K. Ugurbil, "7T vs. 4T: RF power, homogeneity, and signal to noise comparison in head images," *Magn. Reson. Med.*, Vol. 46, No. 1, pp. 24 –30, 2001.

[7] P. F. Van de Moortele, C. Adriany, S. Moeller, J. Ritter, C. M. Collins, M.B. Smith, J. T. Vaughan, and K. Ugurbil, "B1 destructive interferences and spatial phase patterns at 7 T with a head transceiver array coil," *Magn. Reson. Med.*, Vol. 54, No. 6, pp. 1503 – 1518, 2005.

[8] C. A. van den Berg, B. van den Bergen, J. B. Van de Kamer, B. W. Raaymakers, H. Kroeze, L. W. Bartels, and J. J. W. Lagendijk, "Simultaneous B 1+ homogenization and specific absorption rate hotspot suppression using a magnetic resonance phased array transmit coil," *Magn. Reson. Med.*, Vol. 57, No. 3, pp. 577 – 586, 2007.

[9] T. P. A. OReilly, A. G. Webb, and W. M. Brink. "Practical improvements in the design of high permittivity pads for dielectric shimming in neuroimaging at 7T." *J. Magn. Reson. Imaging*, Vol. 270, pp. 108 – 114, 2016.

[10] S. A. Winkler and B. K. Rutt, "Practical methods for improving B1+ homogeneity in 3 tesla breast imaging," *J. Magn. Reson. Imaging*, Vol. 41, No. 4, pp. 992 – 999, 2015.

[11] W. M. Teeuwisse, W. M. Brink, K. N. Haines, and A. G. Webb, "Simulations of high permittivity materials for 7 T neuroimaging and evaluation of a new barium titanate-based dielectric," *Magn. Reson. Med.*, Vol. 67, No. 4, pp. 912 – 918, 2012.

[12] W. M. Brink and A. G. Webb, "A forward model analysis of dielectric shimming in magnetic resonance imaging," Proceedings of the 2013 International Conference on Electromagnetics in Advanced Applications (ICEAA), DOI: 10.1109/iceaa.2013.6632294, 2013.

[13] W. M. Brink, R. F. Remis, and A. G. Webb, "A theoretical approach based on electromagnetic scattering for analysing dielectric shimming in high-field MRI," *Magn. Reson. Med.*, DOI: 10.1002/mrm.25783, 2015.

[14] W. M. Teeuwisse, W. M. Brink, and A. G. Webb, "Quantitative assessment of the effects of high-permittivity pads in 7 Tesla MRI of the brain," *Magn. Reson. Med.*, Vol. 67, No. 5, pp. 1285 – 1293, 2012.

[15] P. de Heer, W. M. Brink, B. J. Kooij, and A. G. Webb, "Increasing signal homogeneity and image quality in abdominal imaging at 3 T with very

high permittivity materials," *Magn. Reson. Med.*, Vol. 68, No. 4, pp. 1317 – 1324, 2012.

[16] P. de Heer, M. B. Bizino, H. J. Lamb, and A. G. Webb, "Improved Cardiac Proton Magnetic Resonance Spectroscopy at 3 T Using High Permittivity Pads," *Invest. Radiol.*, Vol. 51, No. 2, pp. 134 – 138, 2016.

[17] Q. X. Yang, W. Mao, J. Wang, M. B. Smith, H. Lei, X. Zhang, K. Ugurbil, and W. Chen, "Manipulation of image intensity distribution at 7.0 T: passive RF shimming and focusing with dielectric materials," *J. Magn. Reson. Imaging*, Vol. 24, No. 1, pp. 197 – 202, 2006.

[18] W. M. Brink, A. M. A van der Jagt, M. J. Versluis, B. M. Verbist, and A. G. Webb, "High permittivity dielectric pads improve high spatial resolution magnetic resonance imaging of the inner ear at 7T," *Invest. Radiol.*, Vol. 49, No. 5, pp. 271 – 277, 2014.

[19] J. H. F. van Gemert, W. M. Brink, A. G. Webb, and R. F. Remis, "An Efficient Methodology for the Analysis of Dielectric Shimming Materials in Magnetic Resonance Imaging," *IEEE Trans. Med. Imag.*, Vol. 36, No. 2, pp. 666 – 673, 2017.

[20] A. Quarteroni and G. Rozza, Reduced Order Methods for Modeling and Computational Reduction. Vol. 9. Springer, 2014.

[21] A. M. Batson, N. Petridou, D. W. J. Klomp, M. A. Frens, and S. F. W. Neggers, "Single session imaging of cerebellum at 7 Tesla: obtaining structure and function of multiple motor subsystems in individual subjects," *PLOS one*, Vol. 10, No. 8, 2015.

[22] K. R. O'Brien, T. Kober, P. Hagmann, P. Maeder, J. Marques, F. Lazeyras, G. Krueger, and A. Roche, "Robust T1-weighted structural brain imaging and morphometry at 7T using MP2RAGE," *PLOS one*, Vol. 9, No. 6, 2014.

[23] T. Singer, B. Seymour, J. O'Doherty, H. Kaube, R. J. Dolan, and C. D. Frith, "Empathy for pain involves the affective but not sensory components of pain." *Science*, Vol. 303, No. 5661, p. 1157 – 1162, 2004.

[24] A. Favaretto, A. Lazzarotto, D. Poggiali, G. Rolma, F. Causin, F. Rinaldi, P. Perini, and P. Gallo, "MRI-detectable cortical lesions in the cerebellum and their clinical relevance in multiple sclerosis," *Mult. Scler. J.*, Vol. 22, No. 4, 2016.

[25] K. R. O'Brien, A. W. Magill, J. Delacoste, J. P. Marques, T. Kober, H. -P. Fautz, F. Lazeyras, and G. Krueger, "Dielectric pads and low B1+ adiabatic pulses: Complementary techniques to optimize structural T1w wholebrain MP2RAGE scans at 7 Tesla." *J. Magn. Reson. Imaging*, Vol. 40, No. 4 pp. 804 – 812, 2014.

[26] C. J. Stoodley and J. D. Schmahmann, "Functional topography in the human cerebellum: a meta-analysis of neuroimaging studies." *Neuroimage*, Vol. 44, No. 2, pp. 489 – 501, 2009.

[27] C. J. Stoodley and J. D. Schmahmann, "Evidence for topographic organization in the cerebellum of motor control versus cognitive and affective processing." *Cortex*, Vol. 46, No. 7, pp. 831 – 844, 2010.

[28] R. Cabeza and L. Nyberg, "Imaging cognition II: An empirical review of 275 PET and fMRI studies." *Imaging*, Vol. 12, No. 1, p. 1 – 47, 2006.

[29] H. Ito, K. Mori, M. Harada, S. Hisaoka, Y. Toda, T. Mori, A. Goji, Y. Abe, M. Miyazaki, and S. Kagami, " Proton Magnetic Resonance Spectroscopic Study in Autism Spectrum Disorder Using a 3-Tesla Clinical Magnetic Resonance Imaging (MRI) System: The Anterior Cingulate Cortex and the Left Cerebellum," *J. Child Neurol.*, DOI: 10.1177/0883073817702981, 2017.

[30] Z. Yu-Feng, H. Yong, Z. Chao-Zhe, C. Qing-Jiu, S. Man-Qiu, L. Meng, T. Li-Xia, J. Tian-Zia, W. Yu-Feng, "Altered baseline brain activity in children with ADHD revealed by resting-state functional MRI." *Brain and Development*, Vol. 29, No. 2, pp. 83 – 91, 2007.

[31] C. J. Stoodley, E. M. Valera, and J. D. Schmahmann, "Functional topography of the cerebellum for motor and cognitive tasks: an fMRI study." *Neuroimage*, Vol. 59, No. 2, pp. 1560 – 1570, 2012.

[32] K. K. S. Hui, J. Liu, O. Marina, V. Napadow, C. Haselgrove, K. K. Kwong, D. N. Kennedy, and N. Makrisb, "The integrated response of the human cerebro-cerebellar and limbic systems to acupuncture stimulation at ST 36 as evidenced by fMRI." *Neuroimage*, Vol. 27, No. 3, pp. 479 – 496, 2005.

[33] U. S. Inan and R. A. Marshall, *Numerical electromagnetics: the FDTD method*, 1st Edition, Cambridge University Press, 2011, Ch. 4, p. 72.

[34] K. Setsompop, L. L. Wald, V. Alagappan, B. A. Gagoski, and E. Adalsteinsson, "Magnitude least squares optimization for parallel radio frequency excitation design demonstrated at 7 Tesla with eight channels." *Magn. Reson. Med.*, Vol. 59, No. 4 pp. 908 – 915, 2007.

[35] J. Pujol, "The solution of nonlinear inverse problems and the Levenberg-Marquardt method." *Geophysics*, Vol. 72, No. 4 pp. 1– 16, 2007.

[36] A. Christ, "The Virtual Family development of surface-based anatomical models of two adults and two children for dosimetric simulations," *Phys. Med. Biol.*, Vol. 55, No. 2, pp. N23, 2010.

[37] Y. Saad, Iterative methods for sparse linear systems. Vol. 2. Siam, 2003.

[38] W. M. Brink and A. G. Webb, "High permittivity pads reduce specific absorption rate, improve B1 homogeneity, and increase contrasttonoise ratio for functional cardiac MRI at 3 T." *Magn. Reson. Med.*, Vol. 71, No. 4 pp. 1632 – 1640, 2014.

[39] W. M. Brink, M. J. Versluis, J. M. Peeters, P. Bornert, and A. G. Webb, "Passive radiofrequency shimming in the thighs at 3 Tesla using high permittivity materials and body coil receive uniformity correction." *Magn. Reson. Med.*, Vol. 76, No. 6 pp. 1951 – 1956, 2016.

[40] R. A. Lemdiasov, A. A. Obi, and R. Ludwig, "A Numerical Postprocessing Procedure for Analyzing Radio Frequency MRI Coils." *Concepts in Magnetic Resonance Part A*, Vol. 38, No. 4 pp. 113 – 147, 2011.

[41] R. Schmidt and A. G. Webb, "Improvements in RF Shimming in High Field MRI Using High Permittivity Materials With Low Order Pre-Fractal Geometries," *IEEE Trans. Med. Imag.*, Vol. 35, No. 8, pp. 1837 – 1844, 2016.

[42] A. J. E. Raaijmakers, O. Ipek, D. W. J. Klomp, C. Possanzini, P. R. Harvey, J. J. W. Lagendijk, and C. A. T. van den berg, "Design of a Radiative Surface Coil Array Element at 7 T: The Single-Side Adapted Dipole Antenna," *Magn. Reson. Med.*, Vol. 66, No. 5, pp. 1488 – 1497, 2011.